Quantum metrology with precision reaching beyond 1/N-scaling through N-probe entanglement-generating interactions

Xing Deng,[1] Shou-Long Chen,[1] Mao Zhang,[1] Xiao-Fan Xu,[2,*] Jing Liu ⓘ,[1,†] Zhi Gao,[1] Xiao-Chun Duan,[1] Min-Kang Zhou,[1] Lushuai Cao,[1,‡] and Zhong-Kun Hu[1,§]

[1]*MOE Key Laboratory of Fundamental Physical Quantities Measurement, Hubei Key Laboratory of Gravitation and Quantum Physics, PGMF and School of Physics, Huazhong University of Science and Technology, Wuhan 430074, People's Republic of China*
[2]*China Satellite Network Innovation Co., Ltd., Beijing 100029, People's Republic of China*

Nonlinear interactions are recognized as potential resources for quantum metrology, facilitating parameter estimation precisions that scale as the exponential Heisenberg limit of 2^{-N}. We explore such nonlinearity and propose an associated quantum measurement scenario based on the nonlinear interaction of N-probe entanglement-generating form. This scenario provides an enhanced precision scaling of $D^{-N}/(N-1)!$ with $D > 2$ a tunable parameter. In addition, it can be readily implemented in a variety of experimental platforms and applied to measurements of a wide range of quantities, including local gravitational acceleration g, magnetic field, and its higher-order gradients.

I. INTRODUCTION

Quantum metrology aims at improving the practical measurement precisions via quantum advantages. Various measurement scenarios have been proposed [1–3], capable of achieving precisions beyond the standard quantum limit (SQL) of $1/\sqrt{N}$, or even approach the Heisenberg limit $1/N$ for an ensemble of N particles, with nonclassical probe states, such as the entangled [4–7] and squeezed states [8–10], as probe states to interferometers. Besides the nonclassical probe states, quantum parameterization processes based on nonlinear interactions between the probes and the to-be-measured (TBM) system, can also improve the precision by amplifying the phase imprinted by the TBM quantity to the probes. For instance, the nonlinear k-body interaction can reach a precision scaling of N^{-k} ($N^{-k+\frac{1}{2}}$), with (without) entanglement of the probe [11–15], and the nonlinear N-body entanglement-generating interaction can even achieve an exponential Heisenberg limit of 2^{-N} for measuring its interaction strength [16]. These studies support higher than SQL scaling with N for the precision and are broadly applicable.

Despite that the quantum measurement schemes based on the nonlinear interactions can provide the precision with the beyond 1/N-scaling, they suffer from a common constraint of weak applicability, arising from the facts that, the nonlinear interaction coupling the TBM system with the probes is hard to engineer, and more severely, the enhanced precision scaling only works for the measurement of the nonlinear interaction strength, which cannot be assigned to an arbitrary

TBM quantity. To circumvent the constraint, we propose an alternative nonlinear measurement scheme, which can generalize a beyond 1/N-precision scaling to measurements of a wider range of quantities. Instead of introducing a nonlinear interaction between the probes and the TBM system, this measurement scheme deploys the N-body entanglement-generating interaction to locally couple N probes, and we will simply call it N-probe entanglement generation (NPEG) interaction scheme. It will be demonstrated that, for one thing, this NPEG-based scheme maintains the beyond 1/N-precision scaling, and more importantly, once the NPEG interaction is engineered, the nonlinearly coupled probes can be associated to various TBM systems and realize the measurements of different TBM quantities with the improved precision.

The engineering of the NPEG interaction can benefit from the highly developed investigations on effective Hamiltonian engineering. Earlier studies on effective Hamiltonian engineering have been carried out on various platforms, especially in ultracold atomic ensembles for generating effective coupling channels between intrinsically isolated states and tuning the coupling strength. The effective coupling channels are usually engineered via either applying external couplings through lasers [17–20] or by tailoring higher order processes intermediated by energetically detuned states [21–24]. Particularly, nonlinear interactions have been proposed and even experimentally realized [22–26] for the investigations of, e.g., quantum simulations, which could be directly applied for the NPEG-based measurements. The studies on effective Hamiltonian engineering help to lay solid foundation to the NPEG-based measurements, which in turn provide new applications to the engineering studies.

This paper is organized as follows: in Sec. II the NPEG-based measurement scheme is introduced, with an intuitive illustration on the precision scaling; in Sec. III the performance of the NPEG-based measurement scheme, in terms

*xiaofanxu@live.com

†liujingphys@hust.edu.cn

‡lushuai_cao@hust.edu.cn

§zkhu@hust.edu.cn

of the precision scaling, the time resource, the robustness, is analyzed with the quantum and classical Fisher information; in Sec. IV, the applicability of the scheme is investigated with a variety of experimentally realizable setups of the measurement scheme; a summary is present in Sec. V.

II. NPEG MEASUREMENT SCHEME

The key element of the proposed measurement scheme is the NPEG nonlinear interaction, which can be engineered through higher-order processes on various setups [17–27]. We briefly illustrate the engineering procedure with the example of a bosonic system composed of N identical bosons, where each boson can only occupy two states, denoted by $|a\rangle$ and $|b\rangle$. The Hamiltonian of the original system is

$$H_{\text{org}} = \frac{U}{2}(\hat{a}^\dagger\hat{a}^\dagger\hat{a}\hat{a} + \hat{b}^\dagger\hat{b}^\dagger\hat{b}\hat{b}) + j(\hat{a}^\dagger\hat{b} + \hat{a}\hat{b}^\dagger) - \frac{\delta_0}{2}(\hat{n}_a - \hat{n}_b),$$

(1)

in which $\hat{a}/\hat{b}$ ($\hat{a}^\dagger/\hat{b}^\dagger$) annihilates (creates) a boson in the state $|a\rangle/|b\rangle$, and $\hat{n}_a = \hat{a}^\dagger\hat{a}$ ($\hat{n}_b = \hat{b}^\dagger\hat{b}$). In the strong interaction regime with $j \ll U$, the interaction of bosons divides the Hilbert space into a set of subspaces, each of which is composed of energetically resonant basis states of fixed integer number of atoms $N = n_a + n_b$. The states $\{|N, 0\rangle := |\Uparrow\rangle, |0, N\rangle := |\Downarrow\rangle\}$ span such a subspace $\mathbb{S}$, which denote states of all bosons confined in the mode $|a\rangle$ and $|b\rangle$, respectively. Within $\mathbb{S}$, $|\Uparrow\rangle$ and $|\Downarrow\rangle$ are not directly coupled by H_{org}, but an effective coupling between the two states can be engineered through the higher-order process induced by the single-particle hopping j. The resulting effective Hamiltonian (see Appendix A for details) within $\mathbb{S}$ reads

$$H_{\text{eff}} = J_{\text{eff}}(|\Uparrow\rangle\langle\Downarrow| + |\Downarrow\rangle\langle\Uparrow|) - \tfrac{1}{2}\Delta_0(|\Uparrow\rangle\langle\Uparrow| - |\Downarrow\rangle\langle\Downarrow|),$$ (2)

in which the first term is the effective coupling of the nonlinear NPEG form, with $J_{\text{eff}} = \frac{NU}{D^N(N-1)!}$ ($D = U/j$), and the second term is induced by the single-particle detuning with $\Delta_0 = N\delta_0$. While such NPEG interactions have been widely investigated in various fields [21–23,28,29], for the purpose of, e.g., quantum simulations, here we propose that they are also helpful to quantum measurements with improved precision.

The NPEG-based measurement scheme is based on the dynamical process of the many-body correlation induced tunneling (MBCIT), which is a special type of correlated tunneling generalized from the single-particle correlation induced tunneling [30,31]. During the dynamical process, the system periodically oscillate between the initial and the corresponding target, for instance between the state $|+\rangle := (|\Uparrow\rangle + |\Downarrow\rangle)/\sqrt{2}$ and $|\Downarrow\rangle$. Defining $\Gamma := \Delta_0/J_{\text{eff}}$, the probability to be in the state $|\Downarrow\rangle$ during MBCIT from the initial state of $|+\rangle$ is

$$P_\Downarrow(t) = \frac{1}{2} + \frac{\Gamma - \Gamma\cos(\omega t)}{4 + \Gamma^2},$$ (3)

with $\omega = \sqrt{4J_{\text{eff}}^2 + \Delta_0^2}$. The maximum tunneling amplitude $P_\Downarrow^{\text{max}} = \frac{(2+\Gamma)^2}{2(4+\Gamma^2)}$ is reached at the half period, which builds up a dependence between Δ_0 and the experimentally accessible observable $P_\Downarrow^{\text{max}}$. Such dependence permits the estimation of Δ_0, and equivalently δ_0, through the measurement of $P_\Downarrow^{\text{max}}$.
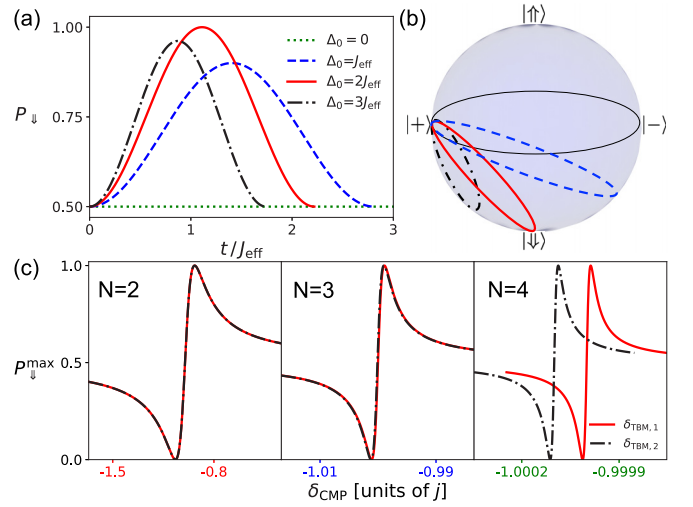

FIG. 1. (a) Time evolution of the probability $P_\Downarrow$ with the initial state $|+\rangle$ for the total detuning $\Delta_0 = 0$ (dotted green line), $\Delta_0 = J_{\text{eff}}$ (dashed blue line), $\Delta_0 = 2J_{\text{eff}}$ (solid red line) and $\Delta_0 = 3J_{\text{eff}}$ (dash-dotted black line). (b) Schematic of evolution trajectories for the initial state $|+\rangle$ with the values of Δ_0 discussed in (a) (lines of the same color correspond to the same value of Δ_0). (c) The maximum tunneling amplitude $P_\Downarrow^{\text{max}}$ as a function of δ_{CMP} under slightly different values of $\delta_{\text{TBM},1}$ and $(1 + 10^{-4})\delta_{\text{TBM},1}$ for $N = 2$ (left panel), $N = 3$ (middle panel), and $N = 4$ (right panel). Here $\delta_{\text{TBM},1}$ is assumed to take the same value of j (j is set to be 1).

The derivative $\partial_{\Delta_0}P_\Downarrow^{\text{max}}$ determines the precision of the estimation, and shows a beyond-exponential dependence on the number of bosons N, implying a beyond $1/N$-scaling of the estimation precision. In Fig. 1(a), the temporal evolutions of $P_\Downarrow(t)$ are depicted for different detunings, and the dependence of the tunneling amplitude on the detuning is illustrated. The MBCIT can also be viewed as an effective precession on the Bloch sphere spanned by $\{|\Downarrow\rangle, |\Uparrow\rangle\}$, as shown in Fig. 1(b), in which H_{eff} plays the role of a biased magnetic field.

The NPEG-based measurement scheme takes each boson in the two-mode system as a probe for measuring the detuning (of some TBM system), specified as δ_{TBM} in the following. Benefiting from the sharp particle-number dependence of $\partial_{\Delta_0}P_\Downarrow^{\text{max}}$ in the MBCIT process, a precision beyond $1/N$-scaling is achieved. Further optimization of the scheme with respect to the value of the detuning itself can also affect the precision, and this optimization is carried out by introducing a compensating of the single-particle detuning, with strength δ_{CMP}, to maximize the measurement precision of δ_{TBM}. The total single-particle and many-body detunings, namely δ_0 and Δ_0, respectively, are then composed of the TBM and the compensate ones, and the TBM detuning can be estimated by $\delta_{\text{TBM}} = \delta_0 - \delta_{\text{CMP}}$, where the total detuning is deduced from the measured $P_\Downarrow^{\text{max}}$. Provided that the value of δ_{CMP} can be obtained with a high enough precision, the precision of δ_{TBM} is determined also to a high precision by that of $P_\Downarrow^{\text{max}}$, which can be optimized by tuning δ_{CMP}.

For a fixed δ_{TBM}, the δ_{CMP} is scanned and the corresponding $P_\Downarrow^{\text{max}}$ is measured, from which the total detuning with the highest precision is deduced. Figure 1(c) plots the response of $P_\Downarrow^{\text{max}}$ to δ_{CMP} in the presence of two slightly different TBM detunings $\delta_{\text{TBM},1}$ (red solid lines) and

$\delta_{\text{TBM},2} = (1 + 10^{-4})\delta_{\text{TBM},1}$ (black dashed lines) for different probe number of $N = 2$ (left panel), $N = 3$ (middle panel), and $N = 4$ (right panel). As calibrated by the colored tick-marks on the x-axis, the response grows sharply as N increases, indicating that the NPEG measurement scheme indeed provides a significant precision improvement with increasing probe number. Meanwhile, it shows that only with $N = 4$ probes can distinguish the two slightly different TBM detunings via statistics from the measured state populations, indicating that the NPEG-based scheme can also enhance measurement resolution. The precision and the resolution with enhanced scaling over the number of probes will benefit realistic metrological scenarios such as gravity and its gradient.

The NPEG-based measurement described above is designed based on a different mechanism from the proposal in Ref. [16] and provides enhanced precision scaling as well as a broader applicability. Since the uncertainty of parameter estimation can be determined by $\Delta\delta = \Delta P/|\partial_\delta P|$, where $\Delta\delta$ and ΔP refer to the uncertainties of the estimated parameter δ and the experimentally measured probability P, respectively, the NPEG-based scheme can simultaneously improve ΔP and $|\partial_\delta P|$, and consequently provides a new precision scaling, as will be demonstrated below. Moreover, in the NPEG-based scheme, once the nonlinear interaction between the probes is realized, the nonlinearly coupled probes can be subjected to different TBM systems and measure different quantities, enabling broad practical applicability of the nonlinear interactions as the quantum resource.

III. OPTIMIZATION AND CHARACTERIZATION

The precision of the NPEG-based measurement can be analyzed and optimized according to the Quantum Cramér-Rao bound [32,33], one of the most well-studied bounds in quantum metrology for both single- [34,35] and multiparameter [36,37] estimations. In this theory, the standard deviation $\delta\delta_0$ is bounded by the inverse of the classical and quantum Fisher information (CFI and QFI), denoted by F_c and F_q, respectively. In the NPEG-based measurement sheme, the maximized CFI and the corresponding precision of δ_0 can be analytically derived as (see Appendix B for details)

$$F_{c,\text{opt}} = \frac{1}{J_{\text{eff}}^2} = \left(\frac{D^N(N-1)!}{NU}\right)^2,$$

$$\delta\delta_0 = \frac{\delta\Delta_0}{N} = \frac{U}{D^N(N-1)!}, \tag{4}$$

indicating the beyond $1/N$-scaling of the precision on the number of probes. The maximized $F_{c,\text{opt}}$ is reached at $(\Delta_0, \omega t) = (0, \pi)$, with the probe state $\cos\frac{\theta}{2}|\Uparrow\rangle + \sin\frac{\theta}{2}|\Downarrow\rangle$ ($\theta \in [0, \pi]$), which lies on the longitude line connecting the states $|\pm\rangle$ in the Bloch sphere. To further check whether the measurement $\{|\Downarrow\rangle\langle\Downarrow|, |\Uparrow\rangle\langle\Uparrow|\}$ is optimal, the QFI under the same condition of the maximized CFI can be derived as

$$F_{q,\text{opt}} = \frac{1}{J_{\text{eff}}^2} = \left(\frac{D^N(N-1)!}{NU}\right)^2, \tag{5}$$

which coincides with $F_{c,\text{opt}}$, meaning that the MBCIT scheme is an optimal measurement scheme to achieve the ultimate

theoretical precision limit, with a beyond $1/N$-scaling behavior [38].

The scaling in Eqs. (4) and (5) is restricted to $\Delta_0 = 0$ and corresponds to the local precision [39], which at first sight might seem to limit the applicability of the NPEG-based scheme. The compensate detuning introduced actually circumvents this restriction. If the compensate detuning can be controlled to high precision, it is always possible to shift the total detuning to $\Delta_0 = 0$ with a fixed Δ_{TBM}, and maintain the overall optimal beyond $1/N$-scaling across all regions. To avoid the high prior information paradox on δ_{TBM}, as discussed in Ref. [40], in practice this process needs to be performed adaptively, such as performing a rough pre-estimation in advance [41]. We will demonstrate with practical examples to show that this prerequisite of the compensate potential with the high controllability can be fulfilled in various practical circumstances and the performance of nonzero Δ_0 will also be thoroughly discussed.

Apart from the minimum value of the precision, the robustness of the achieved precision against imperfect control during measurement is also an important factor in practical quantum metrology [42]. Figure 2 demonstrates the robustness against deviations to the optimized rescaled measurement time ωt and the total detuning Δ_0 [Fig. 2(a)], as well as against the initial state in terms of the relative phase ϕ [Fig. 2(b)]. First, the general behavior of the CFI as functions of Δ_0 and ωt is given in Fig. 2(a) for the probe state $|+\rangle$. It is seen that at $(\Delta_0, \omega t) = (0, \pi)$ F_c reaches the maximum value, and is most stable with respect to the deviations of the detuning and the measurement time. Second, Fig. 2(b) illustrates that for probe states residing on the longitude line of $\varphi = 0$, F_c takes the same maximized value, while the line width of F_c as a function of ωt increases as the probe state approaches $|+\rangle$ (also $|-\rangle$). This indicates that the probe states $|\pm\rangle$ provides the precision of the best robustness with respect to the measurement time. In Fig. 2(c), we further examine F_c and F_q derived from the approximate H_{eff}, with the results numerically calculated by H_{org}. The analytical results based on H_{eff} are found to coincide with numerically obtained ones from H_{org}, which verifies the validity of the analysis based on H_{eff} and confirms the engineered nonlinear NPEG interaction as a useful quantum resource. Besides, it also shows that the performance of the scheme is robust to Δ_0 as in the plot the CFI for $\Delta_0 = \pm 0.5$ is around 89.5% of that for $\Delta_0 = 0$, indicating that the scheme can be well performed adaptively.

The interrogation time is also an important criterion for the performance of different measurement schemes [43,44], thus it is necessary to evaluate how the NPEG interaction benefits the measurement in view of time resource. For this purpose, we compare the time cost to reach the same precision in both linear and nonlinear measurements using the MBCIT process. The linear MBCIT measurement corresponds to loading only a single probe to the measurement procedure and eliminating the nonlinear interaction effect, i.e., taking $N = 1$ in the analysis. The ratio of the time cost to reach the same precision for the linear and the N-probe nonlinear MBCIT measurements, turns out to be $D^{N-1}(N-1)!$ (see Appendix C), which indicates that time cost to reach the same precision also decreases exponentially with N.
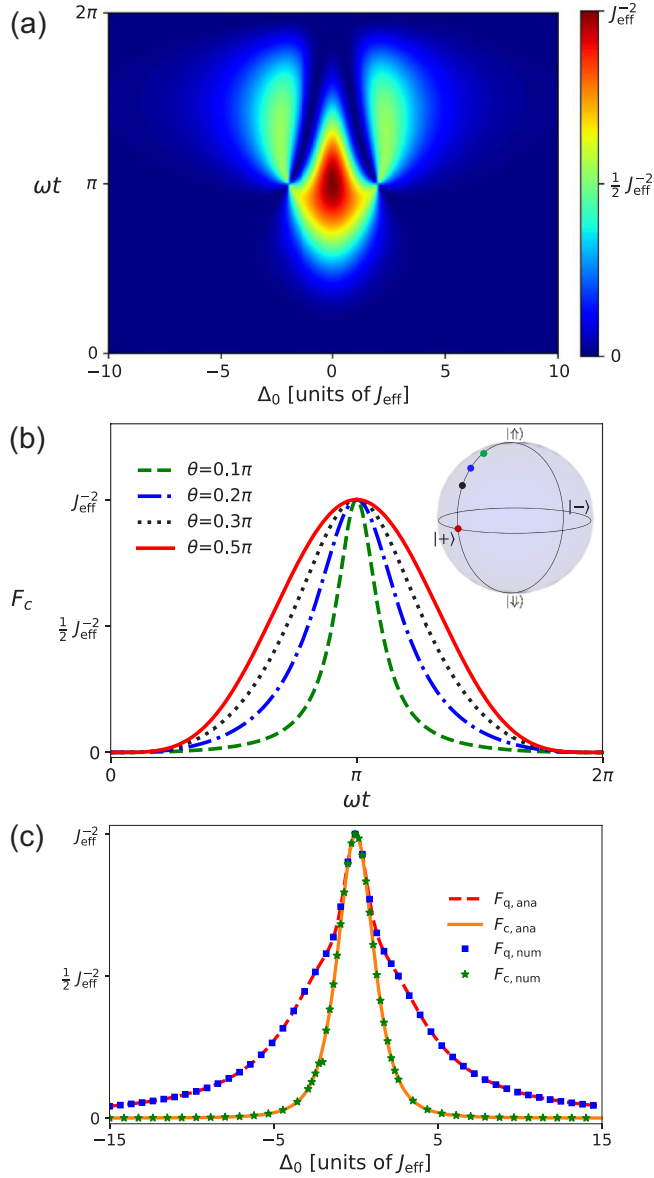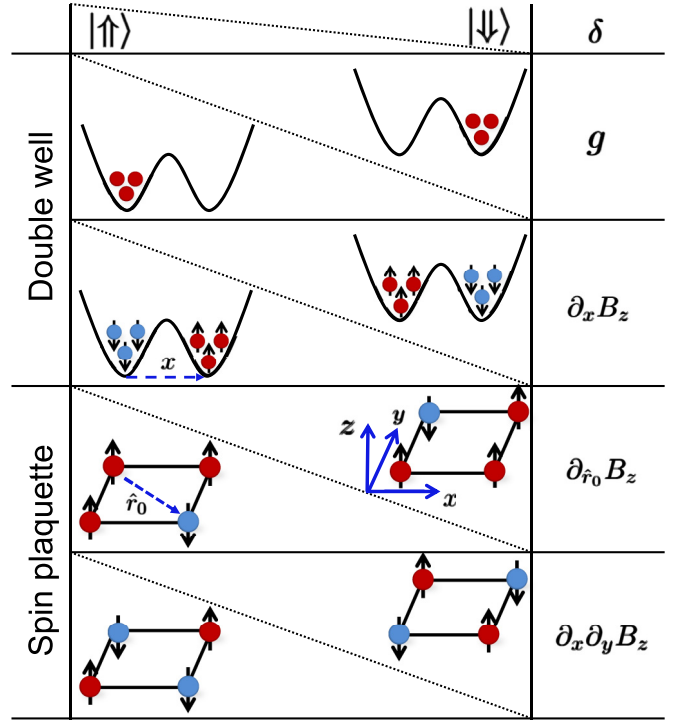
FIG. 3. Schematics of the practical platforms discussed in the main text for performing the MBCIT measurements, with the choice of the probe states and the TBM quantities.

FIG. 2. (a) The CFI F_c as a function of total detuning Δ_0 and ωt for the initial state $|+\rangle$. (b) Time evolution of F_c for the initial states $\sin(\frac{\theta}{2})|\Uparrow\rangle + \cos(\frac{\theta}{2})|\Downarrow\rangle$ with $\theta = 0.1\pi$ (dashed green line), $\theta = 0.2\pi$ (dash-dotted blue line), $\theta = 0.3\pi$ (dotted black line), and $\theta = 0.5\pi$ (solid red line). The insert plot shows the position of these states on the Bloch sphere. (c) The maximum CFI F_c and QFI F_q as a function of Δ_0. The dashed red and solid orange lines are the analytical solutions of F_q and F_c derived via Eq. (2), and the blue squares and green stars are the numerical solutions of F_q and F_c calculated with Eq. (1), respectively. Here N is set to be 4.

IV. APPLICATION SCENARIOS

Besides the beyond $1/N$-scaling, the NPEG-based measurement scheme also enjoys the advantage of the high flexibility, which allows it to be applied to a wide range of quantities. In this section, we present several experimental setups with ultracold atomic ensembles, on which the NPEG-based scheme can be performed to measure different quantities, such as gravity, magnetic field and its gradients.

Our first example explores a system of ultracold atoms confined in a double-well potential, and various nonlinear interactions have been already discussed and investigated in this setup [28,29,45–47], and the NPEG-based measurement scheme can be directly applied. As indicated in the first row of Fig. 3, the NPEG interaction coupling the two many-body states of atoms confined in the subspace of all in the left or right wells, can be engineered by the interplay between the contact interaction and the single-particle hopping. The NPEG-based measurements of the energy detuning between the two wells can be performed, allowing for estimations of gravity acceleration along the orientation of the double well. As illustrated in the second row of Fig. 3, a second type of NPEG interaction can be engineered between spinor atoms confined in the double-well potential [21,22], and couples the states of, for instance, $|\Uparrow\rangle = |\uparrow^{\otimes N}, \downarrow^{\otimes N}\rangle$ and $|\Downarrow\rangle = |\downarrow^{\otimes N}, \uparrow^{\otimes N}\rangle$, where each well is occupied by N atoms, and atoms in different wells are polarized along opposite directions. Such a probe space is insensitive to the net magnetic field and can be used for *in-situ* measurement of the linear magnetic gradient along the orientation of the potential. In both examples, the highly-controllable lasers forming the double well potential can induce compensating detuning with required precision.

The NPEG-based measurement can also be applied to spinor atom plaquette [23,25,26]. In the plaquette, the nonlinear interactions of the NPEG form are realized within different energetically resonant subspaces of the plaquette system, and each such subspace provides a probe space $\mathbb{S}$ for the NPEG-based measurement scheme. The last two rows of Fig. 3 present two probe spaces capable of measuring the

magnetic gradients of different orders. In the configuration that the spin plaquette lies in the xy plane and the TBM magnetic field polarized along the z axis, denoted by $B_z(\vec{r})$, the probe space spanned by $\{|{\uparrow}{\downarrow}{\uparrow}{\uparrow}\rangle, |{\uparrow}{\uparrow}{\uparrow}{\downarrow}\rangle\}$ (indicating the polarization of the four spinors in the plaquette), allows the *in-situ* measurement of the first-order magnetic gradient $\partial_{\hat{r}_0} B_z$, with $\hat{r}_0$ along the diagonal line of the plaquette (slashed line in the third row of Fig. 3). Turning to the probe space of $\{|{\uparrow}{\downarrow}{\uparrow}{\downarrow}\rangle, |{\downarrow}{\uparrow}{\downarrow}{\uparrow}\rangle\}$, the total spin of the probe states is zero, and such a probe space provides a good candidate for the *in-situ* measurement of the second-order magnetic gradient $\partial_x \partial_y B_z$. The spin-dependent lattice potential is also readily implemented in the setup, which can induce the single-particle compensate detuning.

We further take the measurement scenario introduced in the first row of Fig. 3 as an example to quantitatively analyze the performance of the NPEG-based scheme in the practical measurements. We consider an array of double wells, each of which is loaded with N ultracold atoms as the probe. The atoms are subjected to the gravity force and the gravity acceleration g of the Earth is the TBM quantity. In the measurement setup, we consider that the NPEG-based measurements are performed in parallel for $M = 10\,000$ double-well supercells. We calculate the lower-bound uncertainty of measured g as a function of the measurement time t for $N \in [1, 6]$, with all relative parameters taken from the experimental setup in Ref. [48]. As shown in the main figure of Fig. 4, the lower-bound uncertainty $\delta_{\text{lb}}(g)$ monotonically decreases with the measurement time, until reaching a minimum. The minimized $\delta_{\text{lb}}(g)$ corresponds to the optimized Fisher information derived in Eqs. (4) and (5), and the measurement time reaching this minimum is just the optimal measurement time. Moreover, as shown in Fig. 4, increasing N, on the one hand, can exponentially suppress $\delta_{\text{lb}}(g)$, and on the other hand, it increases the measurement time, which bring in a competition in the practical measurements between minimizing the uncertainty and shortening the measurement time. Current experiments on the ultracold atomic dynamics can reach a coherent time over 10 s, and setting the measurement time on this order, one can find that $N = 3$ provides the best lower-bound uncertainty approaching $10\,\mu$Gal, which confirms the NPEG scheme as a source of high precision measurements. Furthermore, assuming that the dynamical coherence time of lattice ultracold atomic experiments can approach the order of 10^3 s in the near future, measurements in a double-well array containing $M = 10\,000$ supercells with each confining $N = 4$ bosons provides the measurement uncertainty below $1\,\mu$Gal. In the insert of Fig. 4, we further plot $\delta_{\text{lb}}(g)\sqrt{t}$ as a function of N, which is a joint measure of the performance with respect to the precision and the time resource. The result illustrates that $\delta_{\text{lb}}(g)\sqrt{t}$ decreases (beyond-)exponentially with N, which further confirms the beyond $1/N$-scaling in the joint viewpoint of precision and the time resource.

The highly developed controllability of ultracold atomic ensembles can facilitate the flexible engineering of the NPEG-type interaction and the compensating detuning with the required precision. The isolation of atomic ensembles from their environment can further suppress the noise induced
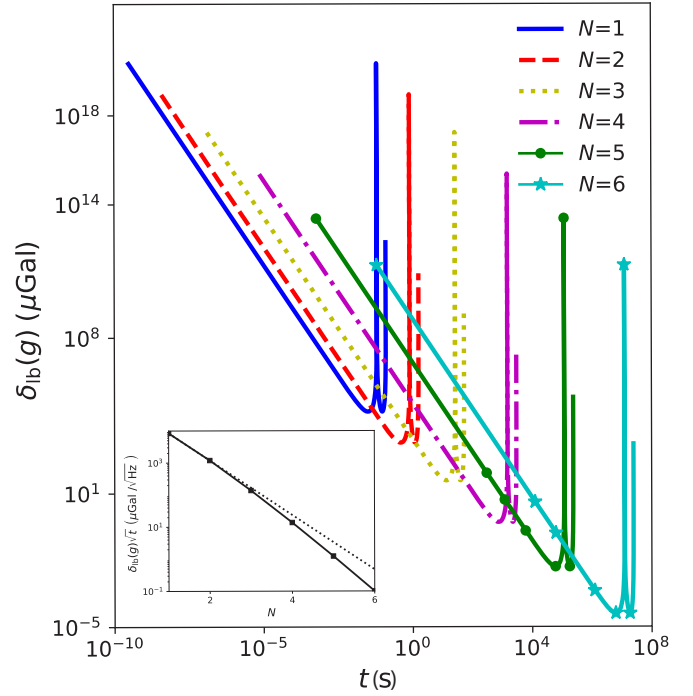

FIG. 4. The lower-bound uncertainty $\delta_{\text{lb}}(g)$ as a function of measurement time t for different particle numbers ($N = 1$ to 6) with $M = 10\,000$ supercells. The parameters are taken from Ref. [48], with the wavelength of the "short" lattices $\lambda_s = 767$ nm, the tunneling $J = 50$ Hz and the interaction $U = 1251$ Hz. The insert shows $\delta_{\text{lb}}(g)\sqrt{t}$ as a function of N, in which the dotted line presents an exponentially decaying curve.

decoherence to a great extent, and guarantees the long enough coherence time for the proposed measurement [49].

V. SUMMARY AND DISCUSSION

We have explored the N-probe entanglement generation interaction as a resource for quantum measurement, and proposed the measurement scheme based on the N-probe entanglement generation-induced many-body correlation-induced tunneling dynamics. We have demonstrated that (i) the N-probe entanglement generation nonlinear interaction manifest itself as a novel measurement resource, which provides an improved precision limit with a beyond $1/N$-scaling of $1/(D^N(N-1)!)$, and (ii) the measurement scheme based on the many-body correlation-induced tunneling process provides a practical and optimal measurement scheme to achieve the beyond $1/N$-scaling.

The N-probe entanglement generation-based measurement scheme not only provides a different mechanism to invoke nonlinearity and leads to a different type of scaling behaviors, its high applicability, as illustrated by the ultracold atomic ensemble, magnetic molecules [50,51], and nuclear-magnetic-resonance setups [52], also facilitates the development of next-generation high-precision apparatuses like gravimeters and magnetometers and benefit both the fundamental and applied science.
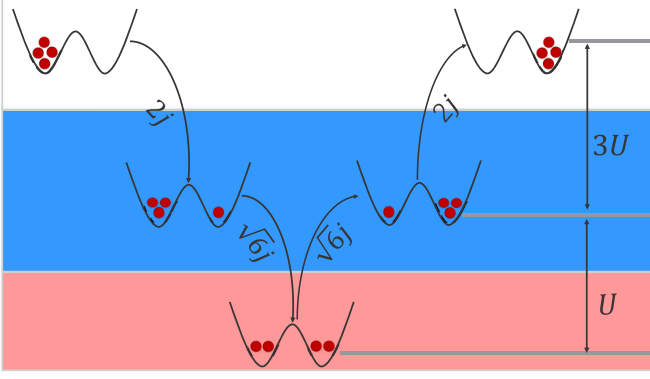
FIG. 5. Pathway of the high-order coupling processes in the high-order perturbation theory for $N = 4$.

APPENDIX A: THE EFFECTIVE HAMILTONIAN

The system of N Bosons in a double-well trap can be described by a two-mode single-band Bose-Hubbard Hamiltonian:

$$H_{\text{org}} = \frac{U}{2}(\hat{a}^\dagger \hat{a}^\dagger \hat{a}\hat{a} + \hat{b}^\dagger \hat{b}^\dagger \hat{b}\hat{b}) + j(\hat{a}^\dagger \hat{b} + \hat{a}\hat{b}^\dagger) - \frac{\delta_0}{2}(\hat{n}_a - \hat{n}_b),$$

(A1)

in which $\hat{a}^{(\dagger)}/\hat{b}^{(\dagger)}$ annihilates (creates) a particle in the state $|a\rangle/|b\rangle$, and $\hat{n}_a = \hat{a}^\dagger \hat{a}$ ($\hat{n}_b = \hat{b}^\dagger \hat{b}$). In the regime of strong

interaction $j \ll U$, the first term of H_{org} denotes the interaction of particles, which divides the complete Hilbert space into different energetically off-resonant subspaces $\{|N - m, m\rangle, |m, N - m\rangle\}$, while each subspaces composed of basis states energetically in resonance with each other. The second term is the one-body hopping term, which builds up higher-order couplings between basis states in each subspace. The last term denotes the energy detuning between $|a\rangle$ and $|b\rangle$. Taking the subspace $\mathbb{S}$ spanned by $\{|N, 0\rangle := |\Uparrow\rangle, |0, N\rangle := |\Downarrow\rangle\}$, and the two base vectors can not be directly coupled with each other, but only by high-order coupling processes, as demonstrated in Fig. 5 for $N = 4$. Actually, all vectors $|N - m, m\rangle$ participate in this high-order coupling processes, and this effective coupling can be evaluated by high-order perturbation theory

$$J_{\text{eff}} = \frac{\prod_{m=0}^{N-1}\langle m, N - m|\hat{H}_J|N - m - 1, m + 1\rangle}{\prod_{m=1}^{N-1}(\langle 0, N|\hat{H}_{\text{int}}|N, 0\rangle - \langle m, N - m|\hat{H}_{\text{int}}|N - m, m\rangle)}$$

$$= \frac{NU}{D^N(N-1)!},$$

(A2)

where $D = U/j$, and $\hat{H}_J$ and $\hat{H}_{\text{int}}$ denotes the hopping and the interaction part of the H_{org}, respectively. Moreover, the third term of H_{org} induces the detuning between the two vectors $|N, 0\rangle$ and $|0, N\rangle$ can be written as $\Delta_0 = N\delta_0$ and the engineered Hamiltonian becomes

$$H_{\text{eff}} = J_{\text{eff}}(|\Uparrow\rangle\langle\Downarrow| + |\Downarrow\rangle\langle\Uparrow|) - \frac{1}{2}\Delta_0(|\Uparrow\rangle\langle\Uparrow| - |\Downarrow\rangle\langle\Downarrow|).$$

(A3)

APPENDIX B: CALCULATIONS OF THE CFI

The temporal evolution of the system during the effective Hamiltonian in Eq. (A3) for a general probe state of $\cos\frac{\theta}{2}|\Uparrow\rangle + e^{i\varphi}\sin\frac{\theta}{2}|\Downarrow\rangle$ ($\theta \in [0, \pi], \varphi \in [0, 2\pi]$) is given by $|\psi(t)\rangle = C_\Uparrow(t)|\Uparrow\rangle + C_\Downarrow(t)|\Downarrow\rangle$, where

$$C_\Uparrow(t) = \cos\left(\frac{\omega t}{2}\right)\cos\left(\frac{\theta}{2}\right) + 2\text{sgn}(J_{\text{eff}})\frac{\sin\left(\frac{\theta}{2}\right)\sin\left(\frac{\omega t}{2}\right)\sin\varphi}{\sqrt{4 + \Gamma^2}} + i\left\{\frac{\text{sgn}(J_{\text{eff}})\sin^2(\frac{\omega t}{2})}{4 + \Gamma^2}\left[\Gamma\cos\left(\frac{\theta}{2}\right) - 2\sin\left(\frac{\theta}{2}\right)\cos\varphi\right]\right\},$$

that is to say, the probability of the measurement $\{|\Downarrow\rangle\langle\Downarrow|, |\Uparrow\rangle\langle\Uparrow|\}$ reads

$$P_\Uparrow(t) = \left[\cos\left(\frac{\omega t}{2}\right)\cos\left(\frac{\theta}{2}\right) + 2\,\text{sgn}(J_{\text{eff}})\frac{\sin\left(\frac{\theta}{2}\right)\sin\left(\frac{\omega t}{2}\right)\sin\varphi}{\sqrt{4 + \Gamma^2}}\right]^2 + \frac{\sin^2\left(\frac{\omega t}{2}\right)}{4 + \Gamma^2}\left[\Gamma\cos\left(\frac{\theta}{2}\right) - 2\sin\left(\frac{\theta}{2}\right)\cos\varphi\right]^2, \quad \text{(B1)}$$

and

$$P_\Downarrow(t) = 1 - P_\Uparrow(t),$$

(B2)

with $\omega = \sqrt{4J_{\text{eff}}^2 + \Delta_0^2}$ and $\Gamma = \Delta_0/J_{\text{eff}}$.

It is generally known that the classical Fisher information F_c can be obtained via $F_c = \sum_i(\partial_x p_i)^2/p_i$ with $\{p_i\}$ a set of probability distribution. For our system,

$$F_c = \frac{(\partial_{\Delta_0}P_\Uparrow)^2}{P_\Uparrow} + \frac{(\partial_{\Delta_0}P_\Downarrow)^2}{P_\Downarrow}.$$

(B3)

Substituting Eq. (B1) into Eq. (B3), we can find that F_c is a function consisting of four parameters, θ, φ, ωt, and Δ_0, and could be written as

$$F_c(\theta, \varphi, \omega t, \Delta_0) = \frac{F_{C1}(\theta, \varphi, \omega t, \Delta_0)}{F_{C2}(\theta, \varphi, \omega t, \Delta_0)}.$$

(B4)

Here $F_{C1}(\theta, \varphi, \omega t, \Delta_0)$ and $F_{C2}(\theta, \varphi, \omega t, \Delta_0)$ are the numerator and denominator of F_c, respectively, and could be expressed as

$$F_{C1}(\theta, \varphi, \omega t, \Delta_0) = 4\{2J_{\text{eff}}\Gamma\cos\theta[2\cos(\omega t) - 2 + (\omega t)\sin(\omega t)] + \sin\theta[J_{\text{eff}}\cos\varphi(\Gamma^2 - 4)(\cos(\omega t) - 1)$$

$$+ \Gamma^2(\omega t)\sin(\omega t)] + \Gamma\sqrt{J_{\text{eff}}^2(4 + \Gamma^2)}[\sin(\omega t) - \omega t\cos(\omega t)]\sin\varphi\}^2, \tag{B5}$$

and

$$F_{C2}(\theta, \varphi, \omega t, \Delta_0) = J_{\text{eff}}^2(4 + \Gamma^2)^2\left\{J_{\text{eff}}^2(4 + \Gamma^2)^2 - \left[J_{\text{eff}}(\Gamma^2 + 4\cos(\omega t))\cos\theta - 4J_{\text{eff}}\Gamma\cos\varphi\sin\theta\sin^2\left(\frac{\omega t}{2}\right)\right.\right.$$

$$\left.\left. + 2\sqrt{J_{\text{eff}}^2(4 + \Gamma^2)}\sin\theta\sin(\omega t)\sin\varphi\right]^2\right\}. \tag{B6}$$

For the initial state $|+\rangle$, which is required for MBCIT, F_c evolves over time as follows:

$$F_c\left(\theta = \frac{\pi}{2}, \varphi = 0, \omega t, \Delta_0\right) = \frac{16\sin^2\left(\frac{\omega t}{2}\right)\left[-\Gamma^2\omega t\cos\left(\frac{\omega t}{2}\right) + (\Gamma^2 - 4)\sin\left(\frac{\omega t}{2}\right)\right]^2}{J_{\text{eff}}^2(4 + \Gamma^2)^2(16 + \Gamma^4 - 2\Gamma^2[\cos(2\omega t) - 4\cos(\omega t) - 1])}.$$

Under this initial state constraint, if and only if $\omega t = \pi$ and $\Delta_0 = 0$, the value of F_c could attain the maximum. Remove this initial state $|+\rangle$ constraint for the optimal condition $\omega t = \pi$ and $\Delta_0 = 0$, i.e., for a general probe state $\cos\frac{\theta}{2}|\Uparrow\rangle + e^{i\varphi}\sin\frac{\theta}{2}|\Downarrow\rangle$ ($\theta \in [0, \pi]$, $\varphi \in [0, 2\pi]$), F_c can be written as follows:

$$F_c(\theta, \varphi, \omega t = \pi, \Delta_0 = 0) = \frac{\cos^2\varphi}{J_{\text{eff}}^2}, \tag{B7}$$

which means that the value of F_c can reach the maximum under $\varphi = 0$ and $\varphi = \pi$ and independent on θ. Then we choose $\varphi = 0$ and $\Delta_0 = 0$ and can obtain the evolution of F_c under different θ,

$$F_c(\theta, \varphi = 0, \omega t, \Delta_0 = 0) = \frac{[\cos(\omega t) - 1]^2\sin^2\theta}{4J_{\text{eff}}^2[1 - \cos^2\theta\cos^2(\omega t)]}, \tag{B8}$$

the robustness of F_c to the measurement time depends on θ and could attain the maximum under $\theta = \pi/2$.

For the above three optimal parameters, i.e., $\theta = \pi/2$, $\varphi = 0$, $\omega t = \pi$, F_c can be written as follows:

$$F_c = \frac{16}{J_{\text{eff}}^2(4 + \Gamma^2)^2}, \tag{B9}$$

and in this optimal parameters, the QFI is calculated as

$$F_q = \frac{16}{J_{\text{eff}}^2(4 + \Gamma^2)^2} + \frac{\Gamma^4\pi^2}{J_{\text{eff}}^2(4 + \Gamma^2)^3}. \tag{B10}$$

Here $F_q \geqslant F_c$, if and only if $\Delta_0 = 0$,

$$F_{c,\text{opt}} = F_{q,\text{opt}} = \frac{1}{J_{\text{eff}}^2} = \left(\frac{D^N(N-1)!}{NU}\right)^2. \tag{B11}$$

The establishment of the equal sign reflects that the MBCIT measurement scheme is optimal.

According to the quantum Cramér-Rao bound [32,33],

$$\delta\Delta_0 \geqslant \frac{1}{\sqrt{\nu F_c}} \geqslant \frac{1}{\sqrt{\nu F_q}}, \tag{B12}$$

where ν is the repetition of experiments. Under the optimized condition,

$$\delta\Delta_0 = |J_{\text{eff}}| = \frac{NU}{D^N(N-1)!}. \tag{B13}$$

Since $\Delta_0 = N\delta_0$,

$$\delta\delta_0 = \frac{\delta\Delta_0}{N} = \frac{U}{D^N(N-1)!}. \tag{B14}$$

APPENDIX C: TIME CONSUMPTION

To show the advantages of this nonlinear MBCIT scheme in the time resource consumption, we compare the time cost to reach the same precision in the nonlinear and linear MBCIT measurements. For the linear MBCIT measurement, which corresponds to the case loading N sing-body probes to the measurement procedure and repeat m_1 measurements, the precision and the time resource consumption could be written as

$$\delta_1 = \frac{|j|}{\sqrt{N m_1}}, \tag{C1}$$

$$\tau_1 = \frac{m_1\pi}{|2j|}. \tag{C2}$$

As for the nonlinear MBCIT measurement, which corresponds to the case loading a N-body probe to the measurement procedure and repeat m_2 measurements, the precision and the time resource consumption could be written as

$$\delta_2 = \frac{|J_{\text{eff}}|}{N\sqrt{m_2}}, \tag{C3}$$

$$\tau_2 = \frac{m_2\pi}{|2J_{\text{eff}}|}. \tag{C4}$$

For the same precision, i.e., $\delta_1 = \delta_2$, the ratio of the time cost turns out to be

$$\frac{\tau_2}{\tau_1} = \frac{1}{D^{N-1}(N-1)!}. \tag{C5}$$

[1] V. Giovannetti, S. Lloyd, and L. Maccone, Quantum Metrology, Phys. Rev. Lett. **96**, 010401 (2006).

[2] V. Giovannetti, S. Lloyd and L. Maccone, Advances in quantum metrology, Nat. Photon. **5**, 222 (2011).

[3] D. Braun, G. Adesso, F. Benatti, R. Floreanini, U. Marzolino, M. W. Mitchell, and S. Pirandola, Quantum-enhanced measurements without entanglement, Rev. Mod. Phys. **90**, 035006 (2018).

[4] V. Giovannetti, S. Lloyd, and L. Maccone, Quantum-enhanced measurements: Beating the standard quantum limit, Science **306**, 1330 (2004).

[5] M. W. Mitchell, J. S. Lundeen, and A. M. Steinberg, Super-resolving phase measurements with a multiphoton entangled state, Nature (London) **429**, 161 (2004).

[6] X.-Y. Luo, Y.-Q. Zou, L.-N. Wu, Q. Liu, M.-F. Han, M. K. Tey, and L. You, Deterministic entanglement generation from driving through quantum phase transitions, Science **355**, 620 (2017).

[7] Y.-Q. Zou, L.-N. Wu, Q. Liu, X.-Y. Luo, S.-F. Guo, J.-H. Cao, M. K. Tey, and L. You, Beating the classical precision limit with spin-1 Dicke states of more than 10 000 atoms, Proc. Natl. Acad. Sci. U.S.A. **115**, 6381 (2018).

[8] D. J. Wineland, J. J. Bollinger, W. M. Itano, and D. J. Heinzen, Squeezed atomic states and projection noise in spectroscopy, Phys. Rev. A **50**, 67 (1994).

[9] C. Groß, Spin squeezing, entanglement and quantum metrology, in *Spin Squeezing and Non-linear Atom Interferometry with Bose-Einstein Condensates* (Springer, Berlin, 2012), pp. 5–23.

[10] H. Bao, J. Duan, S. Jin, X. Lu, P. Li, W. Qu, M. Wang, I. Novikova, E. E. Mikhailov, K.-F. Zhao, K. Mølmer, H. Shen, and Y. Xiao, Spin squeezing of 10^{11} atoms by prediction and retrodiction measurements, Nature (London) **581**, 159 (2020).

[11] J. Beltrán and A. Luis, Breaking the Heisenberg limit with inefficient detectors, Phys. Rev. A **72**, 045801 (2005).

[12] S. Boixo, S. T. Flammia, C. M. Caves, and J. M. Geremia, Generalized Limits for Single-Parameter Quantum Estimation, Phys. Rev. Lett. **98**, 090401 (2007).

[13] S. Choi and B. Sundaram, Bose-Einstein condensate as a nonlinear Ramsey interferometer operating beyond the Heisenberg limit, Phys. Rev. A **77**, 053613 (2008).

[14] M. Napolitano, M. Koschorreck, B. Dubost, N. Behbood, R. J. Sewell, and M. W. Mitchell, Interaction-based quantum metrology showing scaling beyond the Heisenberg limit, Nature (London) **471**, 486 (2011).

[15] X. Nie, J. Huang, Z. Li, W. Zheng, C. Lee, X. Peng, and J. Du, Experimental demonstration of nonlinear quantum metrology with optimal quantum state, Sci. Bull. **63**, 469 (2018).

[16] S. Roy and S. L. Braunstein, Exponentially Enhanced Quantum Metrology, Phys. Rev. Lett. **100**, 220501 (2008).

[17] U. Haeberlen and J. S. Waugh, Coherent averaging effects in magnetic resonance, Phys. Rev. **175**, 453 (1968).

[18] L. M. K. Vandersypen and I. L. Chuang, NMR techniques for quantum control and computation, Rev. Mod. Phys. **76**, 1037 (2005).

[19] N. Goldman and J. Dalibard, Periodically Driven Quantum Systems: Effective Hamiltonians and Engineered Gauge Fields, Phys. Rev. X **4**, 031027 (2014).

[20] A. Eckardt, Colloquium: Atomic quantum gases in periodically driven optical lattices, Rev. Mod. Phys. **89**, 011004 (2017).

[21] H. Pu and P. Meystre, Creating Macroscopic Atomic Einstein-Podolsky-Rosen States from Bose-Einstein Condensates, Phys. Rev. Lett. **85**, 3987 (2000).

[22] H. Pu, W. Zhang, and P. Meystre, Macroscopic Spin Tunneling and Quantum Critical Behavior of a Condensate in a Double-Well Potential, Phys. Rev. Lett. **89**, 090401 (2002).

[23] H.-N. Dai, B. Yang, A. Reingruber, H. Sun, X.-F. Xu, Y.-A. Chen, Z.-S. Yuan, and J.-W. Pan, Four-body ring-exchange interactions and anyonic statistics within a minimal toric-code Hamiltonian, Nat. Phys. **85**, 1195 (2017).

[24] R. C. Brown, R. Wyllie, S. B. Koller, E. A. Goldschmidt, M. Foss-Feig, and J. V. Porto, Two-dimensional superexchange-mediated magnetization dynamics in an optical lattice, Science **348**, 540 (2015).

[25] B. Paredes and I. Bloch, Minimum instances of topological matter in an optical plaquette, Phys. Rev. A **77**, 023603 (2008).

[26] S. Nascimbène, Y.-A. Chen, M. Atala, M. Aidelsburger, S. Trotzky, B. Paredes, and I. Bloch, Experimental Realization of Plaquette Resonating Valence-Bond States With Ultracold Atoms in Optical Superlattices, Phys. Rev. Lett. **108**, 205301 (2012).

[27] H. P. Büchler, M. Hermele, S. D. Huber, M. P. A. Fisher, and P. Zoller, Atomic Quantum Simulator for Lattice Gauge Theories and Ring Exchange Models, Phys. Rev. Lett. **95**, 040402 (2005).

[28] S. Fölling, S. Trotzky, P. Cheinet, M. Feld, R. Saers, A. Widera, T. Müller, and I. Bloch, Direct observation of second-order atom tunnelling, Nature (London) **448**, 1029 (2007).

[29] H.-N. Dai, B. Yang, A. Reingruber, X.-F. Xu, X. Jiang, Y.-A. Chen, Z.-S. Yuan, and J.-W. Pan, Generation and detection of atomic spin entanglement in optical lattices, Nat. Phys. **12**, 783 (2016).

[30] L. Cao, I. Brouzos, B. Chatterjee, and P. Schmelcher, The impact of spatial correlation on the tunneling dynamics of few-boson mixtures in a combined triple well and harmonic trap, New J. Phys. **14**, 093011 (2012).

[31] L. Cao, S. I. Mistakidis, X. Deng and P. Schmelcher, Collective excitations of dipolar gases based on local tunneling in superlattices, Chem. Phys. **482**, 303 (2017).

[32] C. W. Helstrom, *Quantum Detection and Estimation Theory* (Academic Press, New York, 1976).

[33] A. S. Holevo, *Probabilistic and Statistical Aspects of Quantum Theory* (North-Holland, Amsterdam, 1982).

[34] M. G. A. Paris, Quantum estimation for quantum technology, Int. J. Quantum Inform. **7**, 125 (2009).

[35] G. Tóth and I. Apellaniz, Quantum metrology from a quantum information science perspective, J. Phys. A: Math. Theor. **47**, 424006 (2014).

[36] M. Szczykulska, T. Baumgratz, and A. Datta, Multi-parameter quantum metrology, Adv. Phys.: X **1**, 621 (2016).

[37] J. Liu, H. Yuan, X.-M. Lu, and X. Wang, Quantum Fisher information matrix and multiparameter estimation, J. Phys. A: Math. Theor. **53**, 023001 (2020).

[38] S. L. Braunstein and C. M. Caves, Statistical Distance and the Geometry of Quantum States, Phys. Rev. Lett. **72**, 3439 (1994).

[39] M. J. W. Hall and H. M. Wiseman, Does Nonlinear Metrology Offer Improved Resolution? Answers from Quantum Information Theory, Phys. Rev. X **2**, 041006 (2012).

[40] V. Giovannetti and L. Maccone, Sub-Heisenberg Estimation Strategies are Ineffective, Phys. Rev. Lett. **108**, 210404 (2012)

[41] A. A. Berni, T. Gehring, B. M. Nielsen, V. Händchen, M. G. A. Paris, and U. L. Andersen, *Ab initio* quantum-enhanced

optical phase estimation using real-time feedback control, Nat. Photon. **9**, 577 (2015).

[42] C. L. Degen, F. Reinhard, and P. Cappellaro, Quantum sensing, Rev. Mod. Phys. **89**, 035002 (2017).

[43] V. Giovannetti, S. Lloyd, and L. Maccone, Quantum-enhanced positioning and clock synchronization, Nature (London) **412**, 417 (2001).

[44] M. M. Rams, P. Sierant, O. Dutta, P. Horodecki, and J. Zakrzewski, At the Limits of Criticality-Based Quantum Metrology: Apparent Super-Heisenberg Scaling Revisited, Phys. Rev. X **8**, 021022 (2018).

[45] A. M. Dudarev, R. B. Diener, B. Wu, M. G. Raizen, and Q. Niu, Entanglement Generation and Multiparticle Interferometry With Neutral Atoms, Phys. Rev. Lett. **91**, 010402 (2003).

[46] S. Zöllner, H.-D. Meyer, and P. Schmelcher, Few-Boson Dynamics in Double Wells: From Single-Atom to Correlated Pair Tunneling, Phys. Rev. Lett. **100**, 040401 (2008).

[47] Y.-A. Chen, S. Nascimbène, M. Aidelsburger, M. Atala, S. Trotzky, and I. Bloch, Controlling Correlated Tunneling and Superexchange Interactions With ac-Driven Optical Lattices, Phys. Rev. Lett. **107**, 210405 (2011).

[48] B. Yang, H. Sun, C.-J. Huang, H.-Y. Wang, Y.-J. Deng, H.-N. Dai, Z.-S. Yuan, and J.-W. Pan, Cooling and entangling ultracold atoms in optical lattices, Science **369**, 550 (2020).

[49] S. F. Huelga, C. Macchiavello, T. Pellizzari, A. K. Ekert, M. B. Plenio, and J. I. Cirac, Improvement of Frequency Standards With Quantum Entanglement, Phys. Rev. Lett. **79**, 3865 (1997).

[50] T. Lis, Preparation, structure, and magnetic properties of a dodecanuclear mixed-valence manganese carboxylate, Acta Crystallogr. Sect. B **36**, 2042 (1980).

[51] K. Wieghardt, K. Pohl, I. Jibril, and G. Huttner, Hydrolysis products of the monomeric amine complex $(C_6H_{15}N_3)FeCl_3$: The structure of the octameric iron (III) cation of $\{[(C_6H_{15}N_3)_6Fe_8(\mu_3-O)_2(\mu_2-OH)_{12}]Br_7(H_2O)\}Br \cdot 8H_2O^{\dagger}$, Angew. Chem., Int. Ed. Engl. **23**, 77 (1984).

[52] J. Zhang, Z. Lu, L. Shan, and Z. Deng, Synthesizing NMR analogs of Einstein-Podolsky-Rosen states using the generalized Grover's algorithm, Phys. Rev. A **66**, 044308 (2002).